Sustainable Energy, Grids and Networks 32 (2022) 100853

Contents lists available at ScienceDirect

Sustainable Energy, Grids and Networks

journal homepage: www.elsevier.com/locate/segan

Multi-objective control of isolated power systems under different uncertainty approaches☆,☆☆,★

Spyridon Chapaloglou [a,*], Andreas Faanes [b], Damiano Varagnolo [b,d], Elisabetta Tedeschi [a,c]

[a] Department of Electric Power Engineering, Norwegian University of Science and Technology, O.S. Bragstads Plass 2 E, 7034 Trondheim, Norway
[b] Department of Engineering Cybernetics, Norwegian University of Science and Technology, O.S. Bragstads Plass 2 E, 7034 Trondheim, Norway
[c] Department of Industrial Engineering, University of Trento, Via Sommarive, 9, 38123 Povo, Italy
[d] Department of Information Engineering, University of Padova, Via 8 Febbraio, 2, 35122 Padova, Italy

ARTICLE INFO

Article history:
Received 25 October 2021
Received in revised form 26 May 2022
Accepted 7 July 2022
Available online 16 July 2022

Keywords:
Stochastic model predictive control
Scenario approach
Robust control
Isolated power systems
Energy storage systems
Convex optimization

ABSTRACT

This paper proposes and compares a set of multi-objective supervisory controllers for an isolated power system including a gas turbine operating in load following mode as a dominant source of generation, a battery energy storage system, and stochastic renewable generation. It analyzes their capability to coordinate the gas turbine and energy storage to provide isochronous speed control, achieving fast frequency regulation for the local grid, while the gas turbine can still operate with minimum deviation from its optimal loading and the storage system can follow a pre-scheduled reference state of charge trajectory. In more detail, we consider and compare different control strategies to handle model and disturbance uncertainties, including stochastic model predictive control under various parametrizations of the scenario approach, and robust control under the H_∞ paradigm. The various controllers are compared against a benchmark, i.e., a deterministic predictive control strategy. Instead of point-to-point comparisons for some arbitrary cases (i.e., worst-case or expected), empirical distributions of the controller's performance for the whole probability spectrum are derived, leading to more accurate and representative comparisons. The analyzed performance indicators are nominal dynamic performance, constraint violation probabilities, and expected system operation performance. The results indicate the clear superiority of stochastic control over both robust and deterministic control in dealing with both parametric and disturbance uncertainty. Moreover, choosing an appropriate parametrization is shown to be essential to achieve both good nominal performance and lower violations probability, indicating that the superiority of stochastic control comes with the drawback of needing user-defined tuning from the designer.

1. Introduction

Due to constantly stricter regulations towards increasing renewable penetration, maintaining a stable and efficient operation for isolated power systems has become challenging [1]. Based on recent advances in offshore technologies [2], more and more such isolated grids with high renewable penetration are about to be realized [3], and this highlights the need for efficient controls.

The stochastic nature of renewable energy sources (RES) and the low system inertia, induced by replacing traditional synchronous machines with converter interfaced generators, makes the operation of such grids vulnerable to large frequency variations [4–6]. A common and accepted way to mitigate such issues is the integration of energy storage systems (ESS) such as battery energy storage systems (BESS) [4,7–12]. However, increasing the number of controllable components in the grid complicates the multi-input multi-output (MIMO) nature of these systems, exacerbating the chances of encountering multiple contradictory objectives, additional constraints due to safety, and optimal operation requirements. On top of that, uncertainty poses an additional level of difficulty for controlling such grids [13].

In [14,15] the fundamental methods to provide frequency control in isolated power systems by controlling the generator units, are explained in detail. Two main categories are identified, one being the well-known traditional droop control and the other the isochronous control. With the first, generators modify the

☆ Project/research funded by VISTA - a basic research program in collaboration between The Norwegian Academy of Science and Letters, and Equinor.
☆☆ This scientific paper was supported by the Onassis Foundation, Norway - Scholarship ID: F ZP 056-1/2019-2020.
★ This work was supported by BRU21, NTNU's Research and Innovation Program on Digital and Automation Solutions for the Oil and Gas Industry.
* Corresponding author.
E-mail addresses: spyridon.chapaloglou@ntnu.no (S. Chapaloglou), andreas.faanes96@gmail.com (A. Faanes), damiano.varagnolo@ntnu.no (D. Varagnolo), elisabetta.tedeschi@ntnu.no (E. Tedeschi).

https://doi.org/10.1016/j.segan.2022.100853

Nomenclature

Indices

$i = 1 \dots N_c/N_c$	Prediction/Control horizon index
$\omega = 1 \dots N$	Random scenario index
$t = 0 \dots T_{sim}$	Simulation period time index
$k = 1 \dots N_{sim}$	Discrete simulation step index

Power system variables

SoC	State of Charge
Q_b	Battery charge capacity
C_b	Battery energy capacity
P_b	Battery power
P_ℓ	Load power
P_w	Wind power
P_{wt}	Wind turbine power
P_{gt}	Gas turbine power
$\bar{P}_b$	Battery power rating

Optimization variables and parameters

$\boldsymbol{x}$	States vector
$\boldsymbol{u}$	Control input vector
$\boldsymbol{w}$	Disturbance input vector
$\boldsymbol{X}$	States prediction vector
$\boldsymbol{U}$	Control input sequence vector
$\boldsymbol{\Delta U}$	Control input variation vector
$\boldsymbol{W}$	Disturbance prediction vector
$\boldsymbol{Q}$	Weight matrix for states deviation
$\boldsymbol{R}$	Weight matrix for control action deviation
$\boldsymbol{S}$	State of charge prediction vector
$\boldsymbol{P}$	States constraints matrix
$\boldsymbol{c}$	States constraints constants vector
$\boldsymbol{X}_{soc}^{ref}$	State of charge reference vector
$\boldsymbol{L}$	Weight matrix for state of charge deviation
γ	Constant term for control law parametrization
Γ	Constant terms vector for control law parametrization
θ	Proportional term for control law parametrization
Θ	Proportional terms matrix for control law parametrization
ℓ	Weight for state of charge deviation
μ	Weight for standard deviation of state of charge
λ	Battery power to energy capacity ratio
K_{lqr}	LQR state feedback gain
$S(s)$	Sensitivity transfer function
$K(s)$	Controller transfer function
$T(s)$	Complementary sensitivity transfer function
$W_p(s)$	Performance weight transfer function
$W_u(s)$	Controller effort weight transfer function
$W_d(s)$	Robustness weight transfer function

Abbreviations

DMPC	Deterministic Model Predictive Control
SMPC	Stochastic Model Predictive Control
NP	No Parametrization
FP	Full Parametrization
SF	State Feedback parametrization

active power provision in correspondence to the system's frequency deviation and based on the set droop curve, whereas in isochronous mode the rotational speed and thus the frequency of a single or master unit are tightly regulated to their reference values. It is noteworthy that even though droop control facilitates the load sharing among several units, the frequency will not be restored to its nominal value. To achieve that in the absence of interconnection, frequency restoration will depend only on the local generator capabilities and requires that one of them be in isochronous mode. In other words, from a control perspective, droop control corresponds to a proportional controller whereas isochronous operation corresponds to controllers with integral action. In further detail and from a system dynamics perspective, droop control is the main source of damping, necessary for the stability of the system and isochronous control the term encapsulating error accumulation effects and responsible for achieving zero steady state deviation.

For the isochronous case, a frequency variation will be immediately compensated by the generating unit, providing a service equivalent to the secondary frequency restoration in large interconnected systems. However, in contrast to the isochronous operation of a generator for an isolated system, in large interconnected systems such a service is achieved by the system operator, assigning different activation signals and participation factors to all available generators participating in the FRR (Frequency Restoration Reserve) market. Such services are typically activated after the provision of primary control to stabilize the system after a disturbance and on the scale of several seconds to minutes. We also highlight that the actual speed of frequency restoration will depend on the amount of power imbalance and the operational limits of the involved units (ramp constraints and technical maximum).

In [16] gas turbines dynamics are studied along with power systems frequency dynamics, demonstrating the fast-acting behavior of such generators and the isochronous operation capability (response time in the range of seconds). Such a practical case study for an islanded plant (industrial isolated power system) is also provided in [17].

Various types of advanced control methods for load frequency control of isolated power systems have been proposed in literature. In [18] optimal PID controllers were designed to provide load frequency control in microgrid clusters, in [19] a swarm-optimized fuzzy logic was used for robust secondary frequency control of islanded systems, in [20–22] the H_∞ synthesis concept was used to provide robust secondary frequency control in islanded microgrids, in [23] an MPC controller was investigated to provide load frequency control, in [1] a Grey Wolf Optimization was used to provide frequency support by a BESS for an island power system, in [24] a LQR stochastic based control was proposed to provide secondary frequency regulation in an independent microgrid, in [25,26] fractional order MPC and PID were designed correspondingly to provide frequency control for an islanded microgrids or for single area power systems, in [27] an IMC-PID design was investigated for load frequency control.

In the aforementioned studies, the (isolated) power system is modeled as a continuous time linear time-invariant dynamical system and the control performance is typically assessed through load step variations considering either average or worst cases

disturbances. However, the actual empirical distributions are not derived, possibly leading to biased/over-conservative or rather optimistic conclusions. Nevertheless, all the proposed load frequency controllers include an integral part that brings the steady state error to zero in just a few seconds. Such action resembles the isochronous operation provided by single generators when speed and thus frequency are tightly regulated in stand-alone isolated systems. The system's response time highly depends on the various time constants involved (primarily the inertia) and the operational limits (power provision/absorption capability) of the related units. Therefore, for low inertia isolated power systems, response can be faster than large interconnected systems. We note that when secondary level control is designed and assessed (frequency restoration), primary control loops (i.e., droop) can be included in the dynamics of the power system, by modifying the system's damping.

Different approaches can be found in literature for dealing with uncertainty in frequency control of isolated grids. In [7] a standard model predictive control (MPC) algorithm based on a convex QP problem is employed to control an isolated power system containing critical and non-critical loads, diesel generators, BESS, and RES in the form of photovoltaics and wind power generation. The results demonstrates how MPC can effectively manage several objectives, like preserving power balance in the grid and reducing the fuel consumption of the diesel generators. However, this work integrates uncertainty in a simplistic way, by using scenarios with different level of accuracy for the load profile predictions ranging from a perfect forecast and up to approximately 10% deviation. In [10] authors develop a scheduling algorithm for an isolated power system with high penetration of RES which controls the energy production from fossil sources and the power transactions with the main grid in order to maintain power balance and maximize the RES penetration. This yields an alternative strategy to the MPC algorithm and shows good simulation results with a time frame of a day with uncertain forecasts of wind speeds and load profiles. In [28] a stochastic MPC (SMPC) approach that uses scenarios-based description of uncertainties is employed to optimize the fossil energy production and power transactions in the real time market. Such scenarios are generated from a scenario tree designed explicitly to capture the additive feature of uncertainty and avoid infeasibility. The authors of this work compare their algorithm to a so-called prescient optimal control strategy that assumes perfect knowledge of future realizations of the uncertainty, and a certainty equivalent MPC where the uncertain parameters are substituted by average values identified from historical data. Results demonstrate the superiority of the scenario based approach in decreasing costs. [29] performs a comparative study of what they call SMPC and scenario MPC (SCMPC). The difference between the two methods is that the SMPC method converts the probabilistic constraints into deterministic ones using knowledge of the co-variance of the random variables and their propagation along the prediction horizon; the SCMPC approach computes scenarios and forms a scenario tree from the probability distribution of the uncertain variables, as in [28]. The results show that SCMPC generates more realistic scenarios than SMPC because it uses information gathered online to adjust scenario predictions rather than exploiting knowledge on second moments. This accuracy comes though at the cost of increased computational requirements. In [30], the authors develop a scenario SMPC for hybrid vehicles with the goal of improving fuel efficiency while obeying constraints on the state of charge (SoC) of the battery and the power exchanged with it. However, the SCMPC is modified to only generate scenarios that are feasible and likely. The disturbance, i.e., the power requested by the driver, is instead estimated via a Markov chain that predicts the future driver inputs by learning the previous request pattern in real time. Results from [30] show that their SCMPC with learning may outperform classical MPC formulations, and that in many simulations the SMPC performs almost as an MPC with perfect knowledge of future realizations of the disturbances. Other methods consider then a robust control design approach to mitigate uncertain frequency variations [20]. For example, in [31] the authors apply both an H_∞ and μ synthesis approaches for robust frequency control in islanded microgrids. Results show that the two control algorithms may outperform an "optimally tuned" PID controller in the presence of structured uncertainty in the form of wind power generation, solar power generation and uncertain load conditions.

The review above highlights the presence of a plethora of different MPC based methods for either optimal scheduling in isolated power systems or for frequency regulation under uncertainty, either based on robust or stochastic control algorithms. To the best of our knowledge there is though a lack of publicly available studies that analyze how to integrate both tasks into the same control strategy, and thus analyze how control strategies may satisfy optimal schedule tracking while simultaneously ensuring continuous, tight, and fast frequency regulation. The goals of this paper are thus two:

1. propose a series of control formulations and parametrizations (stochastic, robust and deterministic *in primis*) that are all capable of coordinating a master gas turbine and an energy storage to achieve fast frequency regulation for the local grid, while the gas turbine can still operate with minimum deviation from its optimal loading and the storage system can follow a pre-scheduled reference state of charge trajectory;
2. understand which one best handles uncertainties while guaranteeing control performance, and their tradeoffs.

For this purpose, the paper is organized as follows: Section 2 introduces the dynamic MIMO model of the isolated power system, Section 3 describes the design of the controllers we compare, and Section 4 performs the in silico analyses that lead to the main messages given by the paper, i.e., the comparative analysis of the proposed controllers. Lastly, Section 5 draws some final conclusions.

2. Power system modeling

We consider an isolated power system that includes a gas turbine generator in isochronous mode, a wind turbine generator, a battery energy storage system (BESS), and an aggregated load. The gas turbine is mainly responsible to stabilize the system by arresting the frequency deviation after a disturbance and simultaneously cooperate with the BESS to restore it to its nominal value. The following subsections describe then each of these elements in details, assuming the state of the system to be a six-dimensional vector where x_1 and x_2 are states related to the gas turbine (governor and turbine subsystems respectively), x_3 is the power deviation coming form the battery storage system, x_4 is the grid's frequency variation, and x_5, x_6 are the states describing the internal dynamics of the batteries (relaxation and rate capacity effects).

2.1. Modeling of the grid dynamics

Given the scope of this paper, we choose to model the dynamics of the isolated power system as a first order transfer function from power balance to frequency deviation [14,15,32]. The transfer function, derived from the swing equation, is thus

$$M \cdot \frac{d\Delta f(t)}{dt} = -D \cdot \Delta f(t) + \Delta P_g(t) - \Delta P_\ell(t) \tag{1}$$

where M is the inertia constant (due to the generator's rotating mass), D is the damping constant (which encapsulates the combined effects of primary control layer (droop) and load damping, and ΔP_g and ΔP_ℓ the generated and consumed power deviations with respect to the operating point, respectively.

2.2. Gas turbine dynamics

To capture the dynamics of both the turbine and its governor, we model the dispatchable generation system as two first order low pass filters connected in series, giving the equivalent system

$$\begin{bmatrix}\dot{x}_1\\ \dot{x}_2\end{bmatrix} = \begin{bmatrix}-\frac{1}{T_g} & 0\\ \frac{1}{T_t} & -\frac{1}{T_t}\end{bmatrix}\begin{bmatrix}x_1\\ x_2\end{bmatrix} + \begin{bmatrix}\frac{1}{T_g}\\ 0\end{bmatrix} u_1 \tag{2}$$

where T_g is the governor time constant, T_t the turbine time constant, $u_1 = P_{gt}$ the power command to the gas turbine, relatively to its steady state operating point $u_{1|t=0} = \Delta P^*_{gt} = 0$. The input to Eq. (2) is defined as $u_{1|t} = u_{1|t-1} + \Delta u_{1|t}$, from which we see that the part associated to the small signal dynamics of the gas turbine is Δu_1.

2.3. Wind turbine dynamics

The electromechanical conversion on the wind turbine generator is modeled as a first order filter [14,15] from the input (mechanical wind power) to the output (electric power injected into the grid). More precisely, we assume

$$w_1(s) = \frac{\Delta P_w(s)}{sT_{wt} + 1} \tag{3}$$

where T_{wt} is the wind turbine generator time constant, $\Delta P_w(s)$ is the uncertain wind power variation and $w_1(s) = \Delta P_{wt}(s)$ is the corresponding uncertain electric power injections from the wind turbine generator. As for modeling the stochastic process corresponding to the input, or in other words to implement the disturbance model used in our case, we consider wind speed scenarios from a wind speed generator that creates, starting from an average wind speed given as parameter, a realistic set of wind speed samples by means of a physics-driven model of the hydrodynamic effects occurring locally around wind turbines and rotor blades. Such a wind speed samples generator makes use of normal random variables and Kaimal distributions that better capture the small time scale wind intermittency. More details can be found in [33,34].

2.4. Battery energy storage system dynamics

To model the dynamics of the power converter interfacing the battery energy storage system (BESS) with the grid and capture the internal dynamics of the battery cells during charging and discharging processes, we consider the system

$$\begin{bmatrix}\dot{x}_3\\ \dot{x}_5\\ \dot{x}_6\end{bmatrix} = \begin{bmatrix}-\frac{1}{T_B} & 0 & 0\\ 0 & -\frac{c_r}{c_W} & \frac{c_r}{1-c_W}\\ 0 & \frac{c_r}{c_W} & -\frac{c_r}{1-c_W}\end{bmatrix}\begin{bmatrix}x_3\\ x_5\\ x_6\end{bmatrix} + \begin{bmatrix}\frac{1}{T_B}\\ C_b^{-1}\\ 0\end{bmatrix} u_2 \tag{4}$$

where $SoC = x_5 + x_6$ is the state of charge, $u_2 = P_b = u_{2|t=0} + \Delta P_b$ the reference power to the BESS (since $u_{2|t=0} = \Delta P^*_b = 0$ at the steady state), T_B the time constant related to the power conversion and c_r, c_w the coefficients related to the linear modified KiBaM model, illustrated in Fig. 1 and which we assume as sufficiently detailed for our purposes [35–37]. Here it follows a detailed derivation of the proposed simplified battery model based on the modified KiBAM model. The battery charge

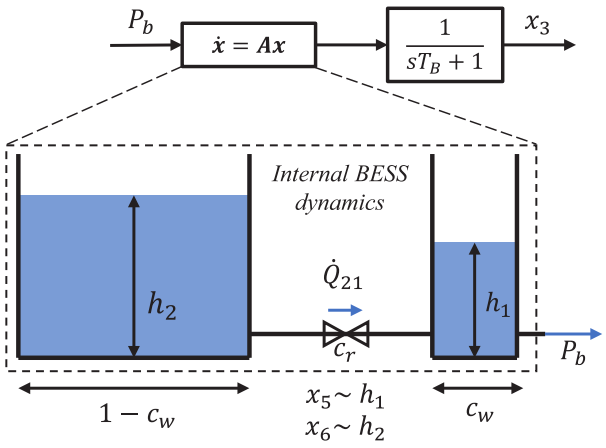

Fig. 1. Modified kinetic battery storage system model (KiBAM) — analogy to coupled water tanks dynamics.

dynamics (rate capacity and charge relaxation effects) can be approximated by an equivalent dynamic system of two interconnected water tanks with different volumes. If Q_b is the total charge of the battery at full capacity, Q_1 and Q_2 the total charge of tank 1 and 2 and their widths c_w and $1 - c_w$ correspondingly we have that $h_1 = \frac{q_1}{c_w}$ and $h_2 = \frac{q_2}{1-c_w}$, where q_1 and q_2 are normalized variables defined as $q_1 = \frac{Q_1}{Q_b}$ and $q_2 = \frac{Q_2}{Q_b}$ and h_1, h_2 represent the normalized water column heights (head) of each tank. Then, considering that the flow across the valve is proportional to the head difference between the two tanks, we can write

$$\dot{Q}_{21} = c'_r (h_2 - h_1) \Rightarrow \dot{q}_{21} = c_r (h_2 - h_1) . \tag{5}$$

where c'_r is the valve's coefficient and $c_r = \frac{c'_r}{Q_b}$. Remembering that the output current is defined as $I_b = \dot{Q}_b$ and based on the above definitions we can write the tanks system equations as

$$\begin{cases}\frac{dQ_1}{dt} &= \dot{Q}_{21} - \dot{Q}_b\\ \frac{dQ_2}{dt} &= -\dot{Q}_{21}\end{cases} \Rightarrow \begin{cases}\dot{q}_1 &= -\frac{c_r}{c_w} q_1 + \frac{c_r}{1-c_w} q_2 - I_b Q_b\\ \dot{q}_2 &= \frac{c_r}{c_w} q_1 - \frac{c_r}{1-c_w} q_2\end{cases} . \tag{6}$$

which can be compactly expressed as

$$\begin{bmatrix}\dot{x}_5\\ \dot{x}_6\end{bmatrix} = \begin{bmatrix}-\frac{c_r}{c_W} & \frac{c_r}{1-c_W}\\ \frac{c_r}{c_W} & -\frac{c_r}{1-c_W}\end{bmatrix}\begin{bmatrix}x_5\\ x_6\end{bmatrix} - \begin{bmatrix}Q_b^{-1}\\ 0\end{bmatrix} I_b \tag{7}$$

where $x_5 = q_1 \sim h_1$ and $x_6 = q_2 \sim h_2$. Then, under the assumption of constant (average) open circuit voltage $\bar{V}_{oc}$ we can express the battery power as $P_b = \bar{V}_{oc} I_b$ and that the battery energy capacity can be written as $C_b = Q_b \bar{V}_{oc}$ [36,37] we have

$$Q_b^{-1} I_b = C_b^{-1} P_b . \tag{8}$$

Finally, neglecting the charge/discharge efficiencies and considering a series-connected first-order delay for the power conversion stage (see Fig. 1) we end up in Eq. (4) where battery power $-\bar{P}_b \le P_b \le \bar{P}_b$ is the system input.

2.5. Dynamics of the whole interconnected system

Combining subsystems Eqs. (1)–(4) as depicted in Fig. 2, letting $x_4 = \Delta f$, and renaming the uncertain power demand as $w_2 = \Delta P_\ell$, Eq. (1) can be rewritten as

$$\dot{x}_4 = -\frac{D}{M} x_4 + \frac{1}{M} (x_2 + x_3 + w_1 - w_2) . \tag{9}$$

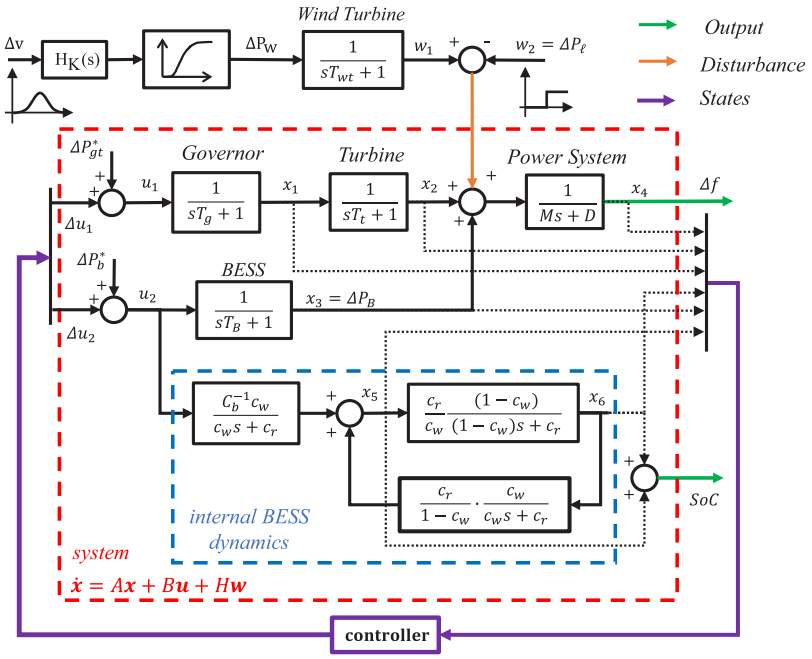

Fig. 2. Schematic representation and modeling of the interconnected system considered in this paper.

This means that the system's model can be written in the state space form

$$\dot{x} = A\boldsymbol{x} + B\boldsymbol{u} + H\boldsymbol{w} \tag{10}$$

$$\mathbf{y} = C^T\boldsymbol{x} \tag{11}$$

where $\boldsymbol{x}^T = [x_1, x_2, x_3, x_4, x_5, x_6]$, $\boldsymbol{u}^T = [u_1, u_2] = [P_{gt}, P_b]$, $\boldsymbol{w}^T = [w_1, w_2] = [\Delta P_{wt}, \Delta P_\ell]$, and

$$A = \begin{bmatrix} -\frac{1}{T_g} & 0 & 0 & 0 & 0 & 0 \\ \frac{1}{T_t} & -\frac{1}{T_t} & 0 & 0 & 0 & 0 \\ 0 & 0 & -\frac{1}{T_B} & 0 & 0 & 0 \\ 0 & \frac{1}{M} & \frac{1}{M} & -\frac{D}{M} & 0 & 0 \\ 0 & 0 & 0 & 0 & -\frac{c_r}{c_W} & \frac{c_r}{1-c_W} \\ 0 & 0 & 0 & 0 & \frac{c_r}{c_W} & -\frac{c_r}{1-c_W} \end{bmatrix} \tag{12}$$

$$B = \begin{bmatrix} \frac{1}{T_g} & 0 \\ 0 & 0 \\ 0 & \frac{1}{T_B} \\ 0 & 0 \\ 0 & -\frac{1}{C_b} \\ 0 & 0 \end{bmatrix}, \quad C^T = \begin{bmatrix} 0 & 0 \\ 0 & 0 \\ 0 & 0 \\ 1 & 0 \\ 0 & 1 \\ 0 & 1 \end{bmatrix}, \quad H = \begin{bmatrix} 0 & 0 \\ 0 & 0 \\ 0 & 0 \\ \frac{1}{M} & -\frac{1}{M} \\ 0 & 0 \\ 0 & 0 \end{bmatrix}. \tag{13}$$

From a block-scheme perspective, the overall system is thus modeled as in Fig. 2.

3. Control design

3.1. Deterministic model predictive control

To achieve optimal operation and reduced fuel usage in isolated power systems, supervisory power management is typically used to deliver the optimal scheduling set points to the local controllers of the different subsystems, such as the BESS and the Gas Turbines [8,38]. In this study we consider integrating the local control objectives of these subsystems along with the frequency regulation of the isolated power system. Local objectives mean that the gas turbine can still operate with minimum deviation from its optimal loading and provide primary grid stabilization while the BESS can still follow a SoC reference trajectory coming from a tertiary dispatch level, and at the same time work together to restore and tightly regulate the system's frequency. For this purpose we propose using a Model Predictive multi-objective multi-input multi-output (MIMO) control that, on top of the basic requirements, aims at minimizing the control effort so to promote reduced actuator wear, and cycling energy storage so to promote longer battery lifetime. To integrate the several control objectives considering the state space model developed Section 2 into a MPC formulation we first use a recursive elimination approach to express the states for the selected prediction horizon N_p as

$$\boldsymbol{X} = A_e\boldsymbol{x}_0 + B_0\boldsymbol{u}_0 + B_e\boldsymbol{\Delta U} + H_e\boldsymbol{W} \tag{14}$$

where $\boldsymbol{x}_0$ is the initial condition, $\boldsymbol{u}_0^T = \left[\Delta P_{gt}^*, \Delta P_b^*\right]$ is the initial operating point of the subsystems and $\boldsymbol{X}$, $\boldsymbol{\Delta U}$, $\boldsymbol{W}$, A_e, B_0, B_e, and H_e are defined in Appendix A. Hence, we define the following qualitative control objectives:

- minimize the frequency deviation (to achieve fast regulation purposes);
- minimize the amplitude of the control signal (to minimize the fuel consumption associated to gas turbine usage);
- perform an optimal system operation (to follow the reference schedule);
- reduce BESS degradation (to minimize replacement costs).

We then translate the above qualitative targets into quantitative ones as follows: first, penalize the states with the Q-norm $\boldsymbol{x}^T Q\boldsymbol{x}$, with Q diagonal and positive definite, so to promote small frequency deviations. Then penalize deviations from operating the gas turbine at its maximum efficiency, and thus penalizing Δu_1 through the norm $\boldsymbol{\Delta u}^T R\boldsymbol{\Delta u}$ to minimize the gas turbine fuel consumption. To follow the reference schedule, penalize the deviations of the state of charge from the reference value using the affine plus quadratic cost $\ell\left(s^T\boldsymbol{x} - SoC_{ref}\right)^2$. Penalizing the BESS degradation can be then promoted in several ways.

Typically, the degradation of a battery is modeled as caused by two distinct effects [39], namely the calendar aging and the cycling effect. Since the cycling degradation is dependent on the number of cycles and the depth of the cycles, a common approach is to discourage cycling by minimizing the standard deviation of the state of charge for the prediction horizon as $\mu\sqrt{\frac{1}{N_p}\sum_{k=1}^{N_p}\left(SoC_k - \frac{1}{N_p}\sum_{k=1}^{N_p} SoC_k\right)^2}$.

Then, by considering the augmented states $\boldsymbol{X}$ and control variables $\boldsymbol{U}$ for the prediction and control horizons (N_p and N_c respectively), and expressing the evolution of state of charge as $\boldsymbol{X}_{soc} = \boldsymbol{S}\boldsymbol{X}$, we can formulate the objective function for the finite horizon optimal control problem as

$$J = \boldsymbol{X}^T\boldsymbol{Q}\boldsymbol{X} + \left(\boldsymbol{S}\boldsymbol{X} - \boldsymbol{X}_{soc}^{ref}\right)^T \boldsymbol{L}\left(\boldsymbol{S}\boldsymbol{X} - \boldsymbol{X}_{soc}^{ref}\right) + \frac{\mu}{\sqrt{N_p - 1}}\left\|\left(\boldsymbol{S}\boldsymbol{X} - \frac{1}{N_p}\|\boldsymbol{S}\boldsymbol{X}\|_1\right)\right\|_2 + \Delta\boldsymbol{U}^T\boldsymbol{R}\Delta\boldsymbol{U} \tag{15}$$

J in Eq. (15) is convex in $\boldsymbol{X}$ and $\Delta\boldsymbol{U}$ by construction (since a sum of basic convex functions. The constraints associated to the problem of optimizing J shall then include the physical limits of the components (like the allowable BESS SoC range, minimum and maximum governor opening, BESS power limits, and ramp rates for the changes of the manipulated variables), and the maximum allowable deviations from the nominal frequency and SoC. Summarizing, the constraints can be expressed mathematically as

$$\boldsymbol{P}\cdot\boldsymbol{X} + \boldsymbol{c} \preceq \boldsymbol{0} \tag{16}$$

$$\boldsymbol{U}_{min} \preceq \boldsymbol{U} \preceq \boldsymbol{U}_{max} \tag{17}$$

$$\Delta\boldsymbol{U}_{min} \preceq \Delta\boldsymbol{U} \preceq \Delta\boldsymbol{U}_{max} \tag{18}$$

where $\boldsymbol{P}$ and $\boldsymbol{c}$ contain information of the hard limits on the states and are presented in Appendix A. Here we note that in practice, different battery cell types and technologies would have different C-rate limitations, resulting in different and tighter bounds on the allowed charge/discharge power. However, such limits can be directly integrated in Eqs. (17) and (18) without affecting the formulation of the problem proposed in this paper. To simplify our analysis while preserving generality, and since the focus of the paper is not on the comparison of different battery types and technologies, we chose to restrict charge/discharge power based on the rated power, as commonly done. This is a simplifying assumption which eventually does not alter the methodology proposed in this paper or the comparative analysis presented later, since all comparisons are performed under the same generic battery model and same constraints. In this way we intend to provide upper theoretical bounds on the performance, while further case specific studies are needed depending on the selected battery technology. As a complement, an additional sensitivity analysis focusing on the different factors that affect the resulting charge/discharge rate is provided in Section 4.5. Eqs. (14)–(18) define then the deterministic model predictive controller (*DMPC*) that will then be compared against the stochastic one defined in the next subsection.

3.2. Stochastic model predictive control

One of the objectives of this manuscript is to investigate which strategy best handles uncertainties while guaranteeing control performance. To account for uncertainties in the control design we then adopt the commonly used scenario approach (*SMPC*) [28–30,40,41], where the cost Eq. (15) from the *DMPC* scheme is replaced by an expectation over the possible outcomes defined from the scenarios. The implementation of such

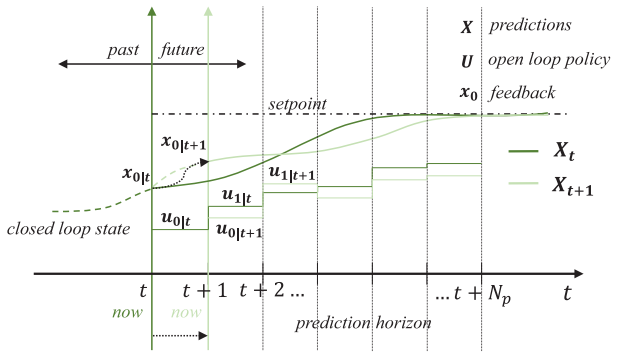

Fig. 3. Feedback mechanism of the open loop MPC policy.

cost function is done through the sample average approximation (SAA) [42] as

$$\mathbb{E}[J(u, w)] \approx \frac{1}{N}\sum_{\omega=1}^{N} J(u_\omega, w_\omega) \tag{19}$$

Where N is the number of scenarios considered. As explained in [41], different constraints are induced by Eqs. (16)–(18) for each random realization of the uncertainty from the randomly sampled uncertainty set. Those can be described as

$$\boldsymbol{P}\cdot\boldsymbol{X}_\omega + \boldsymbol{c} \preceq \boldsymbol{0}, \quad \omega \in \{1, \ldots, N\} \tag{20}$$

$$\boldsymbol{U}_{min} \preceq \boldsymbol{U}_\omega \preceq \boldsymbol{U}_{max}, \quad \omega \in \{1, \ldots, N\} \tag{21}$$

$$\Delta\boldsymbol{U}_{min} \preceq \Delta\boldsymbol{U}_\omega \preceq \Delta\boldsymbol{U}_{max}, \quad \omega \in \{1, \ldots, N\} \tag{22}$$

We highlight, that there is not specific requirement on the distribution of the random variables, or the disturbance model used for the scenario approach, as long as number of samples used is chosen based on the main theorem [43] and the same risk criteria. Another interesting feature related to the SMPC is the different choices for the parametrization of the control input [41], an aspect which is also investigated in this study. In this paper we thus employ different commonly reported controller parametrizations for the SMPC formulation Eqs. (19)–(22), and compare their performance in terms of handling uncertainties and system performance. More specifically, we consider the following parametrizations:

3.2.1. Open loop policy (no parametrization)

The direct open loop policy is also considered as a possible choice for the controller, meaning that the direct output of the solution of the numerical optimization problem Eqs. (19)–(22) is applied to the plant, i.e.,

$$u_i = \gamma_i. \tag{23}$$

The non-parameterized control action (*SMPC-NP*) is also included as a benchmark alternative to better understand and illustrate the effects of the control action parametrization, relatively to a less constrained open loop solution. Here we specify, that still under this parametrization, the controller is of the standard rolling horizon MPC type, which means that feedback of the system's response is given back to the controller in the form of the constantly updated initial condition for each step's optimization problem [44,45]. In that way, no substantial error is accumulated over time. This concept is illustrated in Fig. 3

3.2.2. Affine disturbance feedback

The disturbance feedback full parametrization (*SMPC-FP*) adjusts the control action directly based on past values of disturbance realizations. By using this strategy, the disturbance history is fed into the controller while preserving the convexity of Eq. (19). More in details, such full parametrization is defined as

$$u_i = \gamma_i + \sum_{j}^{i-1} \theta_{i,j} w_{0+j}. \tag{24}$$

With such a parametrization, we include constant terms γ_i and terms $\theta_{i,j}$ proportional to past disturbance realizations w_j, for the specified control horizon. In this way the resulting optimization problem is convex with respect to the control parameters which are iteratively updated on each MPC iteration. Note that, by reorganizing this into a recursive eliminated vector form, and by integrating the number of states, control actions, and disturbances, one obtains

$$\boldsymbol{U} = \Gamma + \Theta \boldsymbol{W} \tag{25}$$

where $\boldsymbol{U}, \boldsymbol{W}, \Gamma, \Theta$ are defined as in Appendix A.

3.2.3. State feedback

Another commonly used controller parametrization for state space formulations is the state feedback parametrization (*SMPC-SF*), defined as

$$u_i = \gamma_i - K_{lqr} x_i \tag{26}$$

where K_{lqr} is a fixed constant. In contrast with *SMPC-FP*, this particular parametrization suffers from the fact that the feedback gain parameter cannot be treated as an optimization variable, since this would result in a non-convex problem [41]. To avoid this issue, K_{lqr} may be chosen to be the infinite horizon optimal gain (see [41] for more details).

3.3. Robust control

To compare the stochastic control approach described in Section 3.2 against a robust control design approach, we also design a mixed synthesis H_∞ controller for the system Eqs. (10) and (11). More precisely we design the H_∞ controller by applying the principles of loop shaping, designing appropriate weights W_p and W_d for acceptable nominal performance and robust stability for the lumped unstructured output multiplicative uncertainty, and finally solving a linear matrix inequality (LMI) optimization problem that minimizes the cost

$$\left\| \begin{bmatrix} W_p S \\ WuKS \\ W_d T \end{bmatrix} \right\|_\infty \leq \gamma \leq 1 \tag{27}$$

where W_p, Wu, and W_d are the disturbance-rejection performance, controller effort and robustness weights respectively. Selecting proper weights for $W_p(s), W_d(s)$ allows then to upper bound the sensitivity $S(s)$ and complementary sensitivity $T(s)$ functions, finding an overall satisfactory controller $K(s)$. This paper follows the basic guidelines from [46] on how to select these weights for robust disturbance rejection; after an iterative procedure we set

$$W_p(s) = \begin{bmatrix} \frac{\frac{2}{3}s+0.01}{s+3.15*10^{-6}} & \frac{\frac{2}{3}s+0.01}{s+3.15*10^{-6}} \\ \frac{\frac{2}{3}s+0.50}{s+4.99*10^{-6}} & \frac{0.32s+0.05}{s+4.74*10^{-6}} \end{bmatrix} \tag{28}$$

$$W_u(s) = 1 \tag{29}$$

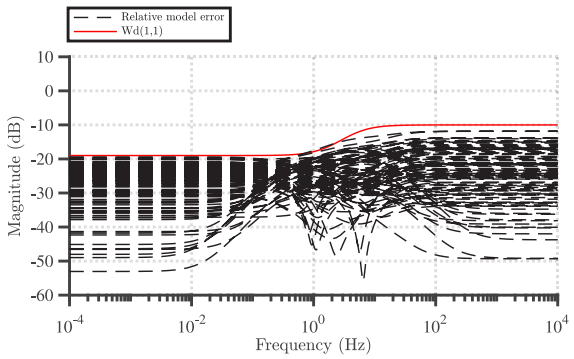

Fig. 4. Frequency response of the relative model error for random realization of uncertainty and robustness weight $W_d(s)$ covering the responses.

$$W_d(s) = \begin{bmatrix} \frac{0.32s+0.018}{s+1.77} & \frac{10s+3.33}{s+33.34} \\ \frac{s+1.00*10^{-8}}{s+100} & \frac{s+3.17}{s+31.65} \end{bmatrix}. \tag{30}$$

From Fig. 4, we notice how the robustness weight selected as

$$W_d(s) = \frac{0.32s + 0.018}{s + 1.77} \tag{31}$$

bounds all realizations of the relative model error of the uncertain plant, validating the required specification for a robust controller design. Note that this type of robust control only considers parametric uncertainty being integrated as output multiplicative.

4. Simulation results and analysis

To analyze the effect of the proposed multi-objective MIMO control strategies, we compare the various control designs described in Sections 3.1 to 3.3 in terms of their dynamic response and capabilities of handling uncertainty. We note that our proposed formulations adopt the simplified but generic battery model described in Eq. (4) where no particular technology-dependent maximum C-rates are enforced besides the power rating limits (Eqs. (17) and (18)). Since the focus of the study is on the comparative analysis and not on the different technologies' comparison, for the purpose of the analysis presented in Sections 4.1 to 4.4 we therefore assume no further technology-dependent battery power constraints, but we ensure the same model and limits for all controllers, for a fair comparison. However, a detailed discussion on the various factors affecting the battery charge/discharge rate and the resulting C-rate is given in Section 4.5. In addition, we note that for the nominal case, the controller assumes no mismatch to the plant model, as to have a benchmark upper bound performance, for comparison with the proposed controllers that assume no knowledge of the nominal plant by considering both the uncertain plant parameters and the unmodeled dynamics. The following key performance indices are defined on the output signals to serve the relative comparison:

- Max frequency deviation:

$$M_f = \|\Delta f(t)\|_\infty \tag{32}$$

- Average (expected) frequency deviation:

$$A_f = \frac{1}{N_{sim}} \sum_{k=1}^{N_{sim}} |\Delta f(k)| \tag{33}$$

- Total fuel usage:

$$T_{u_1} = \sum_{k=1}^{N_{sim}} |\Delta P_{gt}(k)| \tag{34}$$

- Max SoC deviation:

$$M_{soc} = \left\| \boldsymbol{SX} - \boldsymbol{X}^{\boldsymbol{ref}}_{\boldsymbol{soc}} \right\|_{\infty} \tag{35}$$

- Average (expected) SoC deviation:

$$A_{soc} = \frac{1}{N_{sim}} \sum_{k=1}^{N_{sim}} \left| \left(\boldsymbol{SX} - \boldsymbol{X}^{\boldsymbol{ref}}_{\boldsymbol{soc}} \right)_{\boldsymbol{k}} \right| \tag{36}$$

- SoC standard deviation (storage cycling indicator):

$$STD_{soc} = \frac{\left\| \left(\boldsymbol{SX} - \frac{1}{N_{sim}} \left\| \boldsymbol{SX} \right\|_1 \right) \right\|_2}{\sqrt{N_{sim} - 1}} \tag{37}$$

where N_{sim} is the number of simulated time steps.

4.1. Nominal dynamic performance

Initially, we compare the performance of designs *DMPC, SMPC-FP, SMPC-SF, SMPC-NP, H_∞* at the nominal conditions, that is for the nominal set of plant parameters (see Table 1) and for a deterministic knowledge of the disturbance signal (i.e., assuming the uncertain wind power generation to be constant). This means that in this specific case the different versions of the *SMPC* controllers consider only one scenario implying that the *DMPC, SMPC-FP, SMPC-NP* formulations are in this case equivalent. However, the design of the *SMPC-SF* is different since it depends on the state feedback gain K_{lqr} which is calculated independently of the uncertainty realization, thus resulting in a different performance.

The comparison of the dynamic performance of the various designs is illustrated through Fig. 5. In particular, from Fig. 5(a) we can observe the frequency response of the isolated power system, from Fig. 5(b) the SoC regulation to the scheduled value, and from Fig. 5(c) the control effort required from the two subsystems (BESS and gas turbine) to achieve the multiple objectives. From Fig. 5(a) it is clear that the *DMPC/SMPC-FP/SMPC-NP* design achieves the fastest regulation with the smallest peak deviation, the *SMPC-SF* design has the smallest damping and the largest peak deviation while the H_∞ design results in a slower but less oscillatory response. Then, from Fig. 5(b) we observe that H_∞ achieves the best tracking of the reference value with negligible dynamics, while *DMPC/SMPC-FP/SMPC-NP* once more performs better than *SMPC-SF*. However, the performance of H_∞ can be justified by Fig. 5(c) where we can observe the unbalanced use of gas turbine and battery power to achieve the multiple goals. As it is observed, *DMPC/SMPC-FP/SMPC-NP* and *SMPC-SF* split the power usage between the two units whereas H_∞ achieves the same goals by using almost exclusively the gas turbine in a way that avoids the power overshoot in contrast with the others. This sub-optimal response is associated with the tuning of the performance weights, a difficulty which inherently associated with the mixed sensitivity design procedure, since the calculation of the most appropriate weights is a notoriously challenging and tedious task.

4.2. Mixed model and disturbance uncertainty

To further compare the performance of the controllers introduced in Section 4.1 for the nominal conditions, we include a 10% uncertainty in the model parameters, so to capture imperfect knowledge one may have when identifying the system plant parameters. Dynamic simulations were performed for random values of the plant parameters and the corresponding responses as in Fig. 5 where recorded for each design: *DMPC, SMPC-FP, SMPC-SF, SMPC-NP*. The dynamic responses of the system under the various controllers are derived for random realizations of the uncertain parameters and disturbances and compared. By observing Figs. 6 to 10 we see the following patterns:

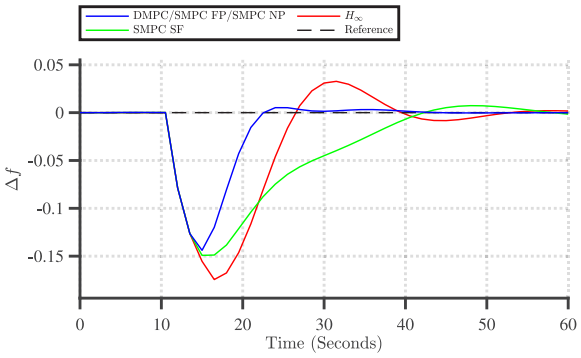

(a) Frequency deviation

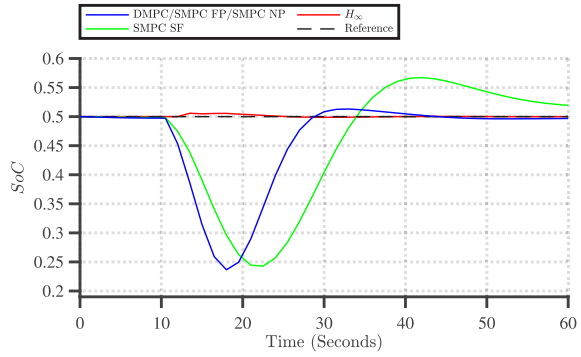

(b) SOC

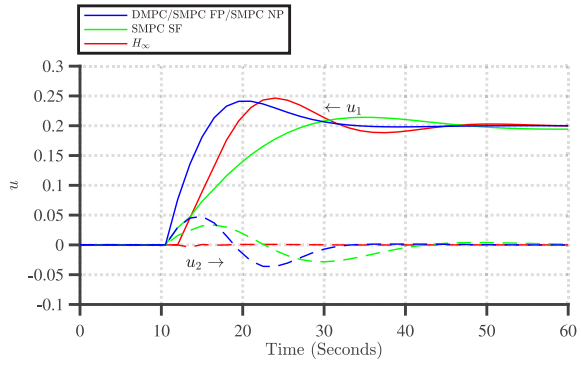

(c) control action

Fig. 5. Response without disturbance and parametric uncertainty.

1. The response profiles of *DMPC* is very similar to the ones of *SMPC-FP, SMPC-NP* since these controllers are somehow equivalent in the absence of disturbance uncertainty.
2. Performance of the *SMPC-SF* are different relatively to the other stochastic controllers, achieving in general less overshoot at the requested gas turbine power, at the cost of slower frequency regulation and an overshot in the SoC tracking.
3. The robust H_∞ controller achieves the best SoC tracking at the presence of small overshoot at the frequency regulation and higher usage of gas turbine power. In addition the gas turbine actuation depends significantly on the plant parameters compared to the other controllers.

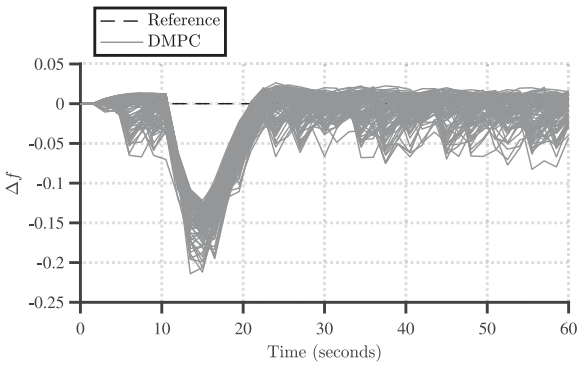

(a) Frequency deviation

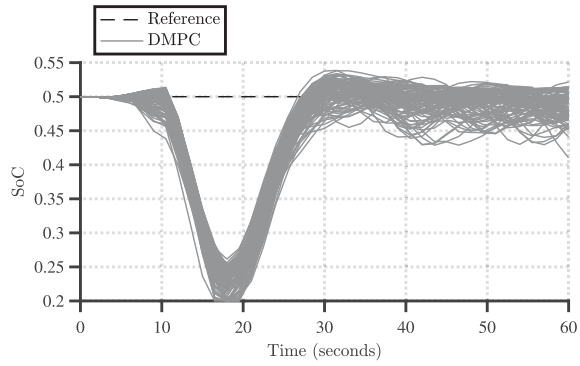

(b) SOC

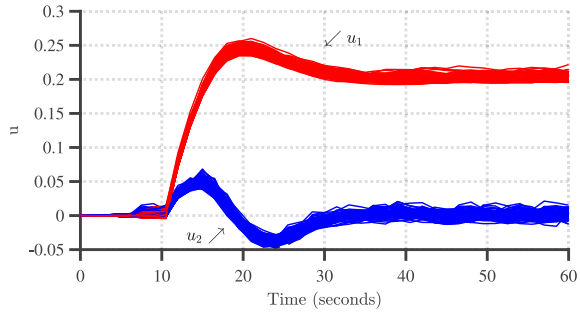

(c) control action

Fig. 6. Response with disturbance and 10% parametric uncertainty for DMPC.

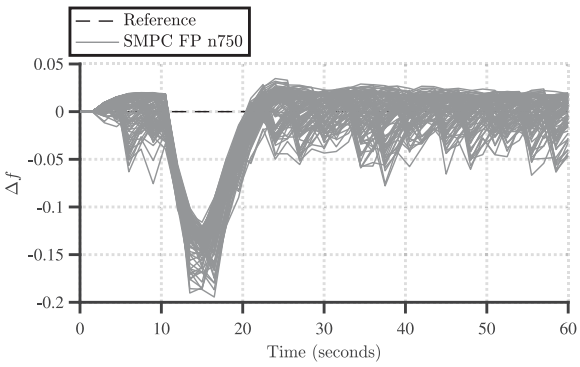

(a) Frequency deviation

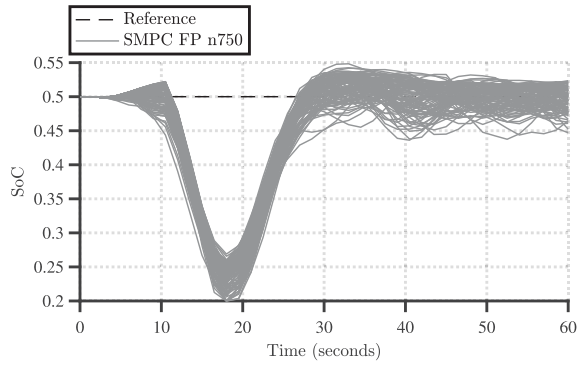

(b) SOC

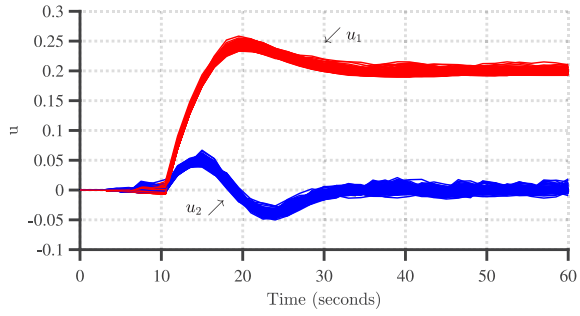

(c) control action

Fig. 7. Response with disturbance and 10% parametric uncertainty for SMPC FP 750 scenarios.

4.3. Monte-Carlo simulations and constraint violation

To assess the ability of the stochastic controllers *SMPC-FP, SMPC-SF, SMPC-NP* in integrating all kinds of uncertainties under the scenario approach, the various designs from Section 4.1 were compared under a Monte-Carlo simulation framework [23,47]. By performing numerous simulations and considering both parametric and disturbance uncertainty, the empirical distributions of the constrain violations and of the indices Eqs. (32)–(37) were calculated.

We note that from the scenario approach, the constraint satisfaction is meant on a probabilistic sense, that is by using specific number of scenarios we can have theoretical guarantees (bound) on the maximum violation probability when the original distribution is used. To demonstrate this effect, the *SMPC-FP* design was considered with different values of scenarios (small number: 250, big number: 750) and corresponding guaranteed violation probabilities. Increasing the number of scenarios generally results in a smaller violation probability, a fact which is numerically validated through Fig. 11 where we observe that for larger number of scenarios the constraint violation probability decreases. From the same figure it is also remarkable to notice the superiority of stochastic control over the deterministic version (*DMPC*) which is always associated with a higher probability of constraint violation. In addition, we can observe that the combined effect of disturbance uncertainty and 10% parametric uncertainty has a greater impact on the max frequency deviation constraint Fig. 11(a) compared to the max SoC deviation constraint Fig. 11(b). From the latter we can see that even though enough cases would imply the maximum allowable deviation, none of them would cause an actual violation.

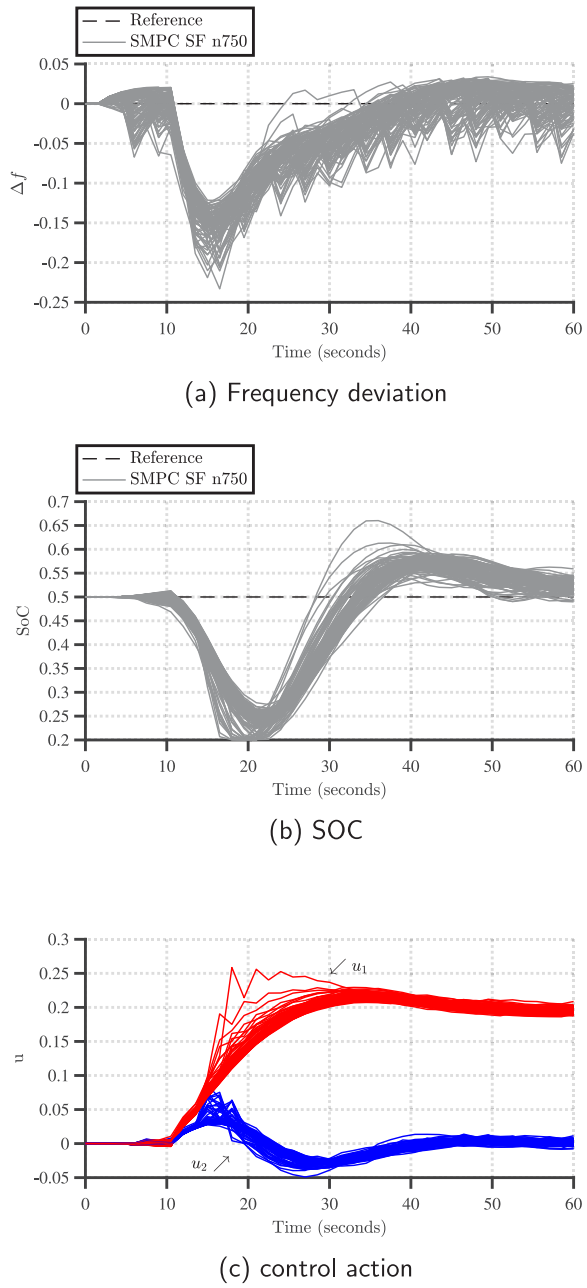

Fig. 8. Response with disturbance and 10% parametric uncertainty for SMPC SF 750 scenarios.

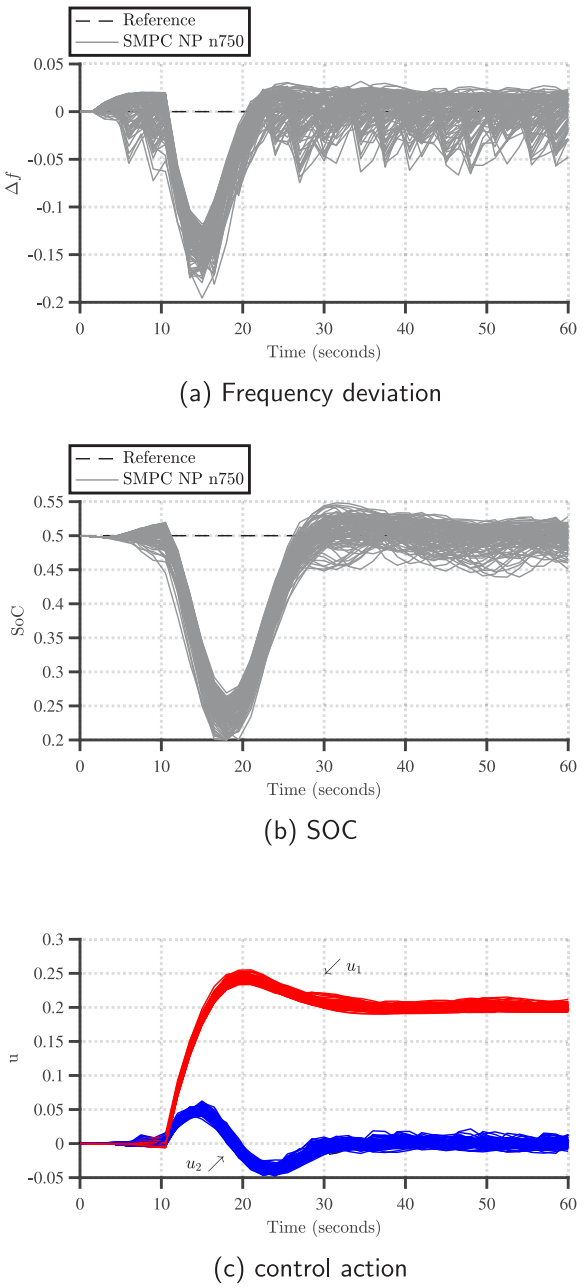

Fig. 9. Response with disturbance and 10% parametric uncertainty for SMPC NP 750 scenarios.

Then, for the large number of scenarios (750) we compared the max constraint violation probabilities for the different controllers (deterministic, stochastic with different parametrizations, and robust). From Fig. 12 we observe that *SMPC-FP* and *SMPC-NP* achieve lower constraint violations for the max frequency and SoC deviations compared to *DMPC* whereas *DMPC* performs better for the max frequency constraint than *SMPC-SF*. This is an interesting result demonstrating (i) the incapability of state feedback to adapt its control law based on disturbance information and (ii) the unexpectedly good performance of the deterministic MPC, considering an expected behavior as the deterministic equivalent. However, the trends seem to be different for the max SoC deviation, where *SMPC-FP* and *SMPC-SF* seem to perform better than *SMPC-NP* and *DMPC*, meaning that the state feedback parametrization has a better capability of handling the parametric uncertainty related to the SoC variations relatively to *DMPC*. Finally, from Figs. 12(a) and 12(b) we observe that the robust design is associated with the highest violation probability in max frequency deviations and the smallest in SoC deviation respectively. This fact is in agreement with the fact that H_∞ considers the parametric uncertainty, minimizing the impact on the SoC deviation but does not considers disturbances that could cause higher frequency variations.

4.4. Expected performance and operation

Finally, the different control designs were compared in terms of their average constraint violation performance, the fuel usage of the gas turbine and the battery cycling. In particular from Fig. 13 we can observe the empirical cumulative distributions of

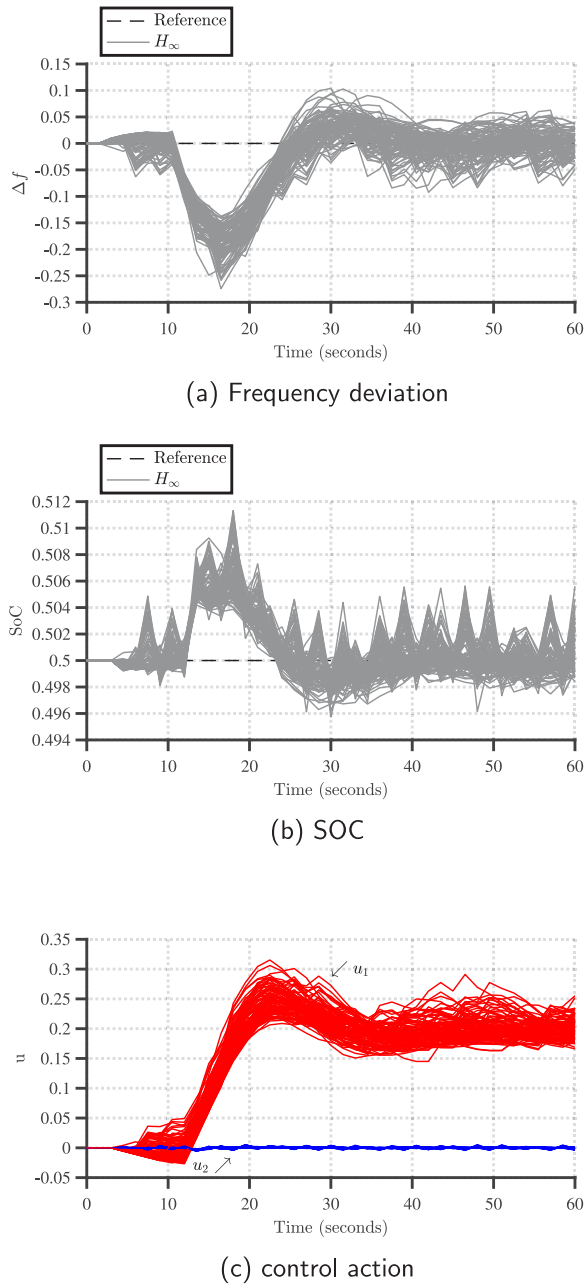

Fig. 10. Response with disturbance and 10% parametric uncertainty for H_∞.

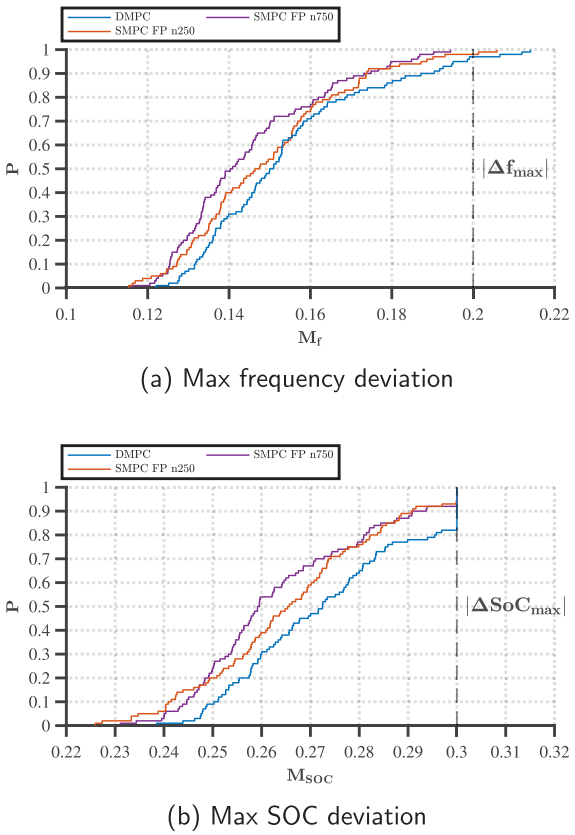

Fig. 11. States empirical cumulative distribution functions with SMPC-FP controller.

the average frequency deviation defined in Eq. (33) and the average SoC deviation as defined in Eq. (36). From Fig. 13(a) we can see that *SMPC-FP, SMPC-NP, DMPC* significantly outperform the *SMPC-SF,* H_∞, with *DMPC* having a bit more violations compared to the best stochastic designs. A similar trend is observed from Fig. 13(b), from which we can see that the average performance of the state feedback control is much worse compared to the other stochastic controllers. From these figures we can also see once more the pattern associated to robust control, where the average frequency violations are even worse than the worst stochastic design while the average SoC deviations are much better compared to the rest.

From Fig. 14 we can observe the effect of each controller on the battery degradation levels. As expected, since the robust control makes minimum use of the storage system, its degradation is the smallest with significant difference from the rest, while for the other controllers we can see again that *SMPC-FP, SMPC-NP* designs have a better degradation performance than *SMPC-SF, DMPC* with *SMPC-SF* again being the worst. However, interestingly the trends reverse for the total fuel usage defined in Eq. (34), where from Fig. 15 we can see that the *SMPC-SF* design is associated with the smallest total fuel usage probability compared to the other designs and the H_∞ is associated with the largest one with a big difference. The other designs (stochastic and deterministic) all have very similar behavior in terms of the total units of fuel distributions.

4.5. Effect of BESS related parameters on the dynamic performance

From the analysis above it is clear that different control methods and parametrizations lead to different dynamic performance of the system. However, it is not only these two factors that affect the system's behavior. Different weighting of the multiple objectives of the MPC optimization problem or different battery characteristics, such as its size, affect the resulting behaviors. Under this perspective, it is worth mentioning that the resulting behaviors shown in the previous sections where all derived for the same weightings and BESS size. The latter was set equal to unity (see Appendix A, Table 1) in order to consider a general case and in accordance with a per unit representation of the power deviations associated with the system operation (see Appendix A). Therefore, the proposed control methodology can be built upon a generic idealized system to remain as general as possible, since the target is not to provide case-specific results but a general control design framework where the control design procedure should be the same irrespectively of the battery capacity.

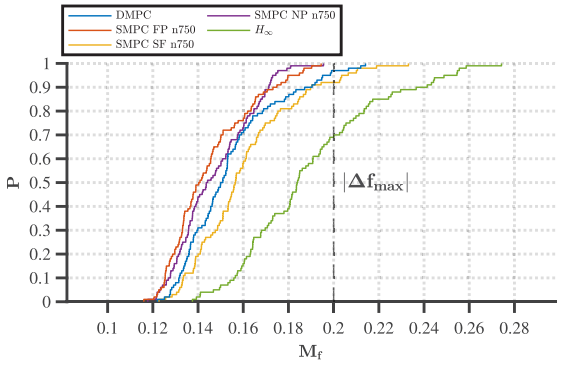

(a) Max frequency deviation

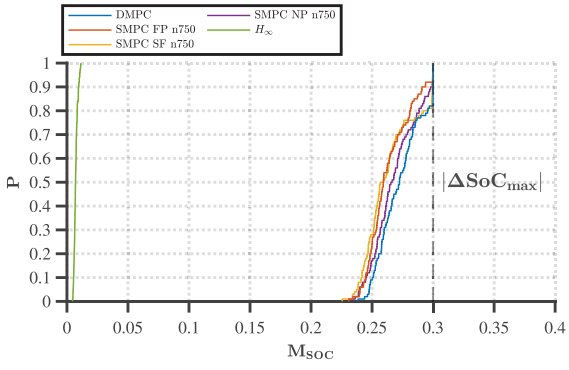

(b) Max SOC deviation

Fig. 12. States empirical cumulative distribution functions SMPC FP vs SMPC SF vs SMPC NP vs DMPC vs H_∞.

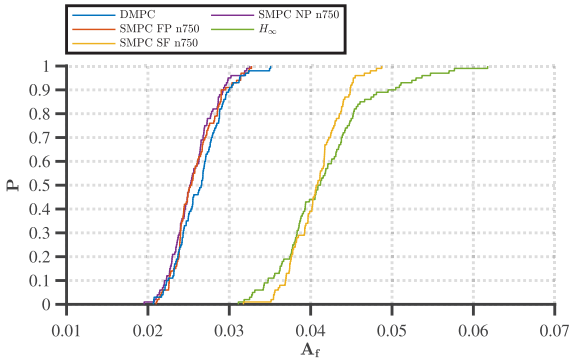

(a) Average frequency deviation

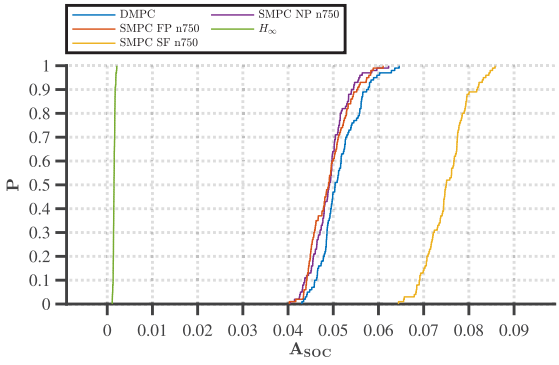

(b) Average SoC deviation

Fig. 13. Average frequency and SOC deviation SMPC FP vs SMPC SF vs SMPC NP vs DMPC vs H_∞.

In particular, when referring to the SoC trajectories observed in the previous sections, it is important to highlight their dependence on 3 main parameters: (i) the SoC deviation weight ℓ, (ii) the energy capacity value C_b and (iii) the maximum power to energy ratio defined as $\lambda = \frac{\bar{P}_b}{C_b}$. Even though the BESS capacity and the power rating are design parameters, whose selection is beyond the scope of this study but requires detailed analyses considering techno-economical perspectives, it is useful to study the effect of those parameters under the proposed MPC framework, for the nominal conditions. For this reason, we performed three individual sensitivity analyses which are explained in detail below. For all the following analyses we follow the same color convention where red represents the SoC deviation, blue the BESS power deviation and green the system's frequency deviation.

4.5.1. Sensitivity analysis for the SoC weighting

First, the effect of the SoC deviation weight ℓ was studied. We performed various simulations (load step disturbance) with increasing values ℓ, giving more significance to large state of charge deviations and thus better constraining the discharge/charge C-rates of the battery. The results are illustrated in Fig. 16. From Fig. 16(a) we observe that increasing ℓ not only leads to less SoC variation but also to decreasing discharging/charging rates, which can be of great importance when specific limits for the C-rates of the battery have to be respected. For example, selecting the maximum value of $\ell = 80$ and considering the battery's discharging at the load step (approximately 2% in 5 s, red curve in Fig. 16(a)) we can estimate a C-rate of around 0.1440, which is much lower than the one for $\ell = 2$. However, putting a lot of weight to the SoC deviation comes at the cost of a higher overshoot at the systems frequency response, as can be observed

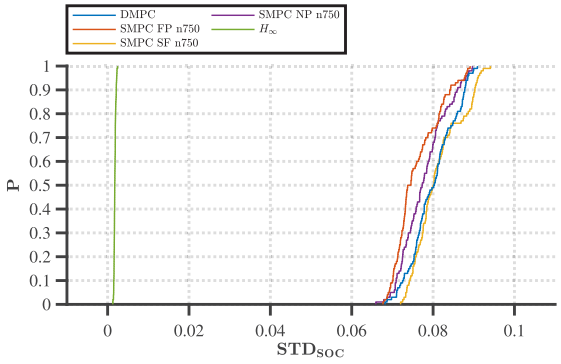

Fig. 14. SoC standard deviation (BESS cycling indicator) SMPC FP vs SMPC SF vs SMPC NP vs DMPC vs H_∞.

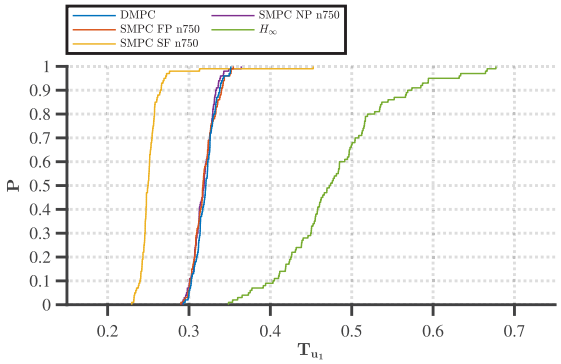

Fig. 15. Total units of fuel SMPC FP vs SMPC SF vs SMPC NP vs DMPC vs H_∞.

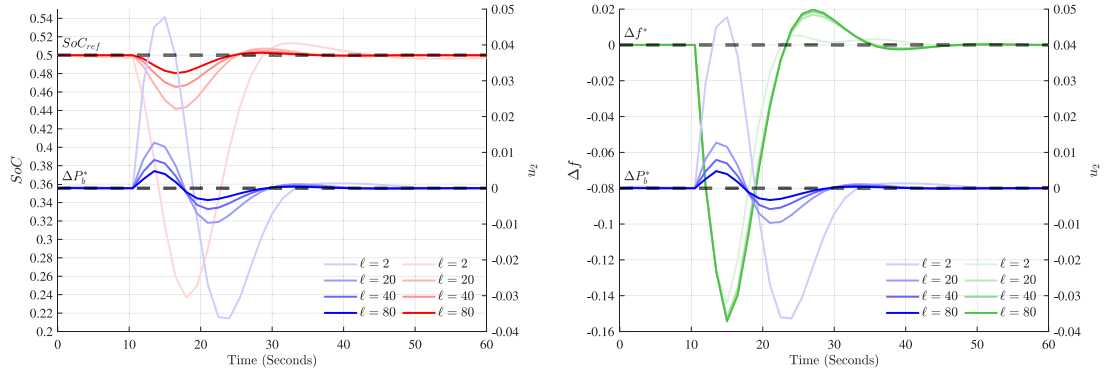

(a) State of charge and battery power deviations (b) System frequency and battery power deviations

Fig. 16. Sensitivity analysis results for varying ℓ. (For interpretation of the references to color in this figure legend, the reader is referred to the web version of this article.)

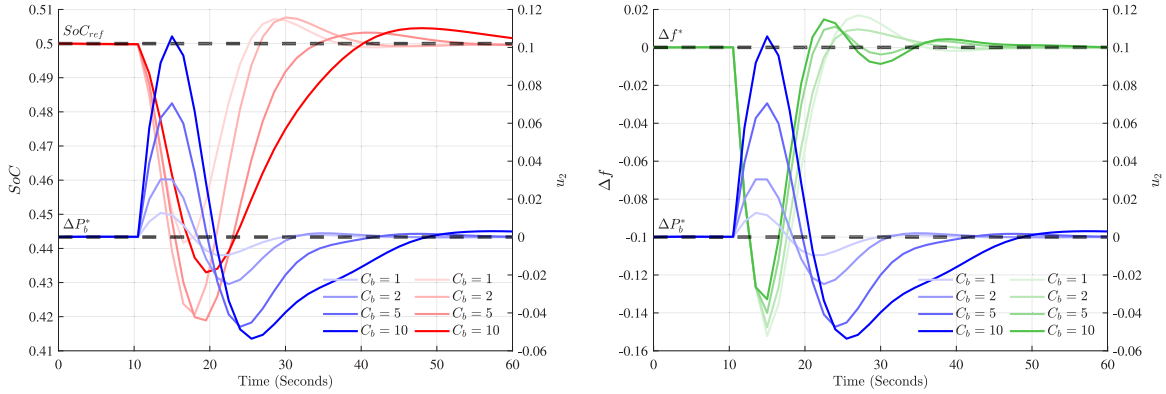

(a) State of charge and battery power deviations (b) System frequency and battery power deviations

Fig. 17. Sensitivity analysis results for varying C_b.

from Fig. 16(b) (bold green line). From this analysis, we can conclude that a value of $\ell = 20$ would give a fair trade-off between the SoC deviation penalization and a realistic C-rate for the battery charging/discharging process. For this reason, we kept this value for the next analyses.

4.5.2. Sensitivity analysis for the BESS capacity

Another very important factor affecting the resulting charge/discharge rates is the total available energy capacity of the battery system. It is expected that for larger capacities and same discharge levels, the C-rates will be decreasing. Again we performed various simulations (load step disturbance) where the BESS per unit scaled capacity C_b is changing in multiples of the nominal one ($C_b = 1$). In Figs. 17(a) and 17(b) we observe the resulting trajectories of the SoC, the BESS power and the system's frequency response. We see that increasing the battery size, the minimum value of SoC is increasing, leading to lower peak C-rate and higher minimum frequency deviation, even though the frequency response is a less dumped. In other words, increasing the battery size, the system can tolerate higher discharge power rates, resulting in lower C-rates for the battery and improved frequency nadir.

4.5.3. Sensitivity analysis for the BESS power to energy ratio

Finally, the effect of the maximum power to energy ratio was studied by varying the λ parameter from 1 to 0.1. This means that a BESS with $\lambda = 1$ has 10 times higher power provision capability than the one for $\lambda = 0.1$, for the given (same) energy capacity. In other words, λ reflects the effect of further restricting the battery charge/discharge power $\bar{P}_b$, resembling different technologies with different C-rate limits which are effectively power constraints. Then, from Fig. 18(a) we observe that by increasing λ we can effectively reduce the C-rate of the BESS not only by reducing its minimum SoC deviation but also by slowing down the BESS response, meaning that to reach its minimum SoC deviation value, more time is required. It is remarkable in that case, since the goalsẃeights were kept to the same values, that the controller requested more power from the BESS for lower λ values, resulting in almost identical system frequency response (Fig. 18(b)). However, this is only available when the power rating of the BESS is large enough (as in our case) not to saturate the requested power.

5. Discussion and conclusions

This study proposed, analyzed and compared a set of multi-objective MIMO supervisory controllers for isolated power systems composed of a gas turbine, a wind turbine and a battery energy storage system. The proposed controllers are all based on the concept of integrating optimal frequency regulation for the isolated grid (isochronous operation) while at the same time tracking scheduling commands for the energy storage system. This was achieved though different model predictive controllers accounting for different types of uncertainty and different controller parametrizations. Overall, the goal has been of comparing deterministic MPC approaches against stochastic MPC ones and robust control.

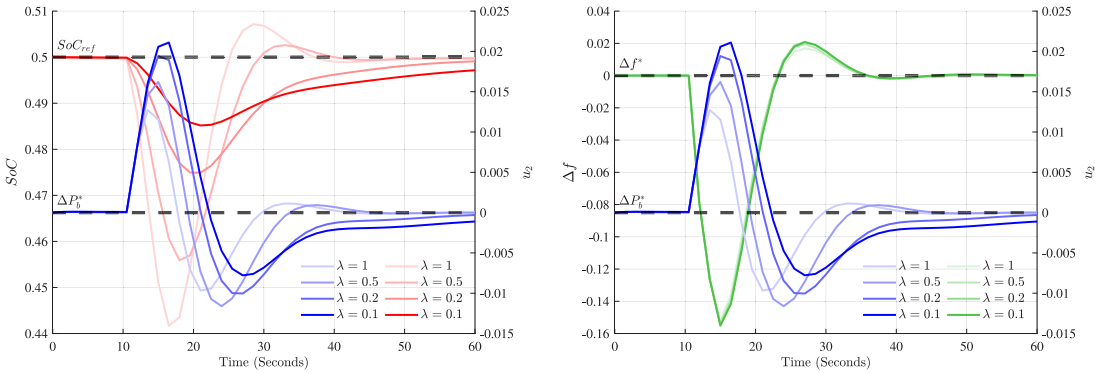

(a) State of charge and battery power deviations

(b) System frequency and battery power deviations

Fig. 18. Sensitivity analysis results for varying λ.

The results showed that stochastic control is *not* always associated with smaller constraint violation probability compared to the deterministic case. The occurrence of this event was, though, strongly correlated on the controller parametrization. In particular, we found that an affine disturbance parametrization is almost always associated with lower violations probabilities and very close to the open loop optimal policy (i.e., no parametrization of the controller). In addition, state feedback was found to be worse not only in terms of nominal performance but also in terms of constraint violation even when compared to the deterministic MPC. However a state feedback approach resulted in the smallest fuel consumption — at the cost though of slower regulation. Last but not least, the analyzed H_∞ robust controller was found resulting in higher constraint violations and sub-optimal coordination of the different subsystems, revealing the need for specialized tuning.

As for possible future work, higher parametric uncertainty could be considered for the comparison of the various proposed controllers and check to what extend the comparison results match the one presented in this study. In addition, higher fidelity simulation models could be used to further validate the results of the comparative analysis, while different specific battery technologies could also be examined for application suitability, given actual C-rate restrictions. Finally, a controller with risk aversion capabilities (i.e. by reducing the number of scenarios in the scenario approach) could be designed and be included in the comparison study.

CRediT authorship contribution statement

Spyridon Chapaloglou: Conceptualization, Methodology, Software, Writing – original draft. **Andreas Faanes:** Validation, Visualization, Software, Writing – original draft. **Damiano Varagnolo:** Supervision, Writing – review & editing. **Elisabetta Tedeschi:** Supervision, Writing – review & editing.

Declaration of competing interest

The authors declare that they have no known competing financial interests or personal relationships that could have appeared to influence the work reported in this paper.

Appendix A

$$\boldsymbol{X}^T = [\boldsymbol{x}_{\tau+1}^T, \dots, \boldsymbol{x}_{\tau+N_p}^T]$$

$$\boldsymbol{U}^T = [\boldsymbol{u}_{\tau+0}^T, \dots, \boldsymbol{u}_{\tau+N_c}^T]$$

$$\boldsymbol{\Delta U}^T = [\boldsymbol{\Delta u}_{\tau+0}^T, \dots, \boldsymbol{\Delta u}_{\tau+N_c}^T]$$

$$\boldsymbol{W}^T = [\boldsymbol{w}_{\tau+0}^T, \dots, \boldsymbol{w}_{\tau+N_c}^T]$$

$$A_e = \begin{bmatrix} A \\ A^2 \\ \vdots \\ A^{N_p} \end{bmatrix}, \quad B_0 = \begin{bmatrix} B \\ AB + B \\ \vdots \\ \sum_{i=1}^{N_p} A^{N_p - i} B \end{bmatrix},$$

$$B_e = \begin{bmatrix} B & 0 & \cdots & 0 \\ AB + B & B & \cdots & 0 \\ \vdots & \vdots & \ddots & \vdots \\ \sum_{i=1}^{N_p} A^{N_p - i} B & \sum_{i=2}^{N_p} A^{N_p - i} B & \cdots & \sum_{i=1+N_c}^{N_p} A^{N_p - i} B \end{bmatrix},$$

$$H_e = \begin{bmatrix} H & 0 & \cdots & 0 \\ AH & H & \cdots & 0 \\ \vdots & \vdots & \ddots & \vdots \\ A^{N_p - 1} H & A^{N_p - 2} H & \cdots & A^{N_p - N_p} H \end{bmatrix}$$

$$\boldsymbol{Q} = \begin{bmatrix} Q_{\tau+1} & 0 & 0 \\ 0 & \ddots & 0 \\ 0 & 0 & Q_{\tau+N_p} \end{bmatrix}$$

$$\boldsymbol{R} = \begin{bmatrix} R_{\tau+1} & 0 & 0 \\ 0 & \ddots & 0 \\ 0 & 0 & R_{\tau+N_c} \end{bmatrix}$$

$$\boldsymbol{s}^T = [0, 0, 0, 0, 1, 1]$$

$$\boldsymbol{S} = \begin{bmatrix} \boldsymbol{0}_{(1-1)\cdot 6+4} & 1 & 1 & \boldsymbol{0}_{(N_p-1)\cdot 6} \\ \boldsymbol{0}_{(2-1)\cdot 6+4} & 1 & 1 & \boldsymbol{0}_{(N_p-2)\cdot 6} \\ \vdots & \vdots & \vdots & \vdots \\ \boldsymbol{0}_{(N_p-1)\cdot 6+4} & 1 & 1 & \boldsymbol{0}_{(N_p-N_p)\cdot 6} \end{bmatrix}$$

$$P = \begin{bmatrix} 0 & 0 & 0 & 1 & 0 & 0 \\ 0 & 0 & 0 & -1 & 0 & 0 \\ 0 & 0 & 0 & 0 & 1 & 1 \\ 0 & 0 & 0 & 0 & -1 & -1 \end{bmatrix}$$

$$\boldsymbol{P} = \begin{bmatrix} P_{\tau+1} & 0 & 0 \\ 0 & \ddots & 0 \\ 0 & 0 & P_{\tau+N_p} \end{bmatrix}$$

$$\boldsymbol{L} = \begin{bmatrix} \ell_{\tau+1} & 0 & 0 \\ 0 & \ddots & 0 \\ 0 & 0 & \ell_{\tau+N_p} \end{bmatrix}$$

$$c = \begin{bmatrix} -\Delta f_{max} \\ \Delta f_{max} \\ -SoC^{ref} - \Delta SoC_{max} \\ SoC^{ref} - \Delta SoC_{max} \end{bmatrix}$$

$$\boldsymbol{c}^T = [c^T_{\tau+0}, \ldots, c^T_{\tau+N_p}]$$

$$\boldsymbol{X}^{ref\,T}_{soc} = [SoC^{ref}_{\tau+0}, \ldots, SoC^{ref}_{\tau+N_p}]$$

$$\Gamma^T = [\boldsymbol{\gamma_1}, \ldots, \boldsymbol{\gamma_{Nc}}]$$

$$\Theta = \begin{bmatrix} \mathbf{0} & \mathbf{0} & \ldots & \mathbf{0} \\ \boldsymbol{\theta_{1,0}} & \mathbf{0} & \ddots & \mathbf{0} \\ \vdots & \ddots & \ddots & \mathbf{0} \\ \boldsymbol{\theta_{Nc-1,0}} & \ldots & \boldsymbol{\theta_{Nc-1,Np-2}} & \mathbf{0} \end{bmatrix}$$

$$\boldsymbol{\gamma_i^T} = [\gamma_{i,1}, \gamma_{i,2}]$$

$$\boldsymbol{\theta_{i,j}^T} = [\theta_{i,j,1}, \theta_{i,j,2}]$$

$$N_{sim} = \frac{T_{sim}}{\Delta t}$$

Table 1
Table of constants.

Parameter	Symbol	Value	Units
Nominal plant			
Governor time constant	$T_{g,0}$	0.05 [8]	[s]
Turbine time constant	$T_{t,0}$	0.5 [8]	[s]
Wind turbine time constant	$T_{WTG,0}$	0.04 [8]	[s]
BESS time constant	$T_{B,0}$	0.1 [8]	[s]
Battery capacity	$C_{b,0}$	1	[p.u.]
Charging well width	$c_{W,0}$	0.93 [36]	[–]
Charging well conductance	$c_{r,0}$	$2.24 \cdot 10^{-5}$ [36]	[–]
Load damping	D_0	1 [8]	$\left[\frac{p.u.}{Hz}\right]$
Inertia constant	M_0	3 [8]	$\left[\frac{p.u.s}{Hz}\right]$
Wind turbine power curve			
Cut in speed	V_{ci}	13	$\left[\frac{m}{s}\right]$
Cut off speed	V_{co}	17	$\left[\frac{m}{s}\right]$
Rated wind speed	V_r	15.5	$\left[\frac{m}{s}\right]$
Rated power	P_r	0.2	[p.u.]
MPC constrains			
Max power deviation	$\mathbf{u_{min}}$	-1	[p.u.]
Min power deviation	$\mathbf{u_{max}}$	1	[p.u.]
Max power increment	$\Delta\mathbf{u_{max}}$	0.5	[p.u.]
Min power increment	$\Delta\mathbf{u_{min}}$	-0.5	[p.u.]
Max frequency deviation	Δf_{max}	0.2	[p.u.]
Max SoC deviation	ΔSoC_{max}	0.3	[p.u.]
Simulation parameters			
Control horizon	N_c	4	[–]
Prediction horizon	N_p	10	[–]
Discrete time step	Δt	1.5	[s]
Simulation length	T_{sim}	60	[s]

Table 2
MPC optimization solution time.

variables #	*SMPC-FP*	*SMPC-SF*	*SMPC-NP*
	32	8	8
N	Optimization solution time [s]		
200	4.97	2.03	2.21
400	9.14	3.16	2.74
600	14.95	4.95	3.78
800	22.19	6.63	5.17
1000	29.12	8.58	6.80

Appendix B

This paper presents a design methodology (proposed multi-objective controller) and a preliminary comparative analysis of various designs either with respect to the way uncertainty is considered (deterministic vs. robust vs. stochastic) or for different control parametrizations for the scenario-based MPC (SMPC). The scenario approach [40,41,43,48] gives the designer the unique capability to leverage risk of violating unseen constraints (from the randomly sampled scenarios). That means that we can reduce the number of scenarios considered by accepting higher risk for the sake of decreasing the controller's computational complexity and therefore the required calculation time. Under this perspective, we performed an analysis investigating the required time for the optimization problem to be solved, for different number of scenarios. The results are given in Table 2. Such times are recorded when using our available computational resources, a 2010 MacBook Pro with 2.4 GHz Intel Core 2 Duo processor, where just a single core was used (not parallel computing). We also not that the recorded execution times include several internal processes of the Matlab-based modeling system for convex optimization (CVX) and interactions with the selected simulation environment Matlab-Simulink. CVX is loaded with numerous additional tasks other than solving the problem itself, such as interpreting the high-level modeling language into numerical matrices, loading searching and accessing those and many other staff that are not open to the user.

In practice, increasing the number of scenarios we include more constraints to the optimization problem, making its solution harder. As we see from the table above, even for relatively low number of scenarios, the required solution time can be significant, giving rise to potential real-time implementation issues. The computational time to solve the optimization problem highly depends on the availability of computational resources which, from a system operator point of view, will not probably be a deadlock, since advanced computing may already be there as it is necessary for other tasks, too. While in the simulation environment there is always sufficient time for the optimization problem to be solved before the next simulation iteration, in a real time implementation non-sufficient time for the problem solution would result in a significant delay which is ignored in the simulations. Therefore, the results presented in this study can be thought of as an upper bound of the controller's performance and further studies are required to investigate what the required computational resources are and what parallelization techniques should be considered before the real-time implementation of the controllers proposed in this theoretical/numerical study.

References

[1] K.S. El-Bidairi, H.D. Nguyen, T.S. Mahmoud, S.D.G. Jayasinghe, J.M. Guerrero, Optimal sizing of Battery Energy Storage Systems for dynamic frequency control in an islanded microgrid: A case study of Flinders Island, Australia, Energy 195 (2020) 117059, http://dx.doi.org/10.1016/j.energy.2020.117059.

[2] R. Itiki, S.G. Di Santo, C. Itiki, M. Manjrekar, B.H. Chowdhury, A comprehensive review and proposed architecture for offshore power system, Int. J. Electr. Power Energy Syst. 111 (2019) 79–92, http://dx.doi.org/10.1016/j.ijepes.2019.04.008.

[3] Electrification of oil and gas operations, 2021, URL https://www.equinor.com/en/what-we-do/electrification.html.

[4] T. Yang, Y. Zhang, Z. Wang, H. Pen, Secondary frequency stochastic optimal control in independent microgrids with virtual synchronous generator-controlled energy storage systems, Energies 11 (9) (2018) http://dx.doi.org/10.3390/en11092388.

[5] H. Bevrani, B. Francois, T. Ise, Microgrid Dynamics and Control, 2017, http://dx.doi.org/10.1002/9781119263739.

[6] T. Kerdphol, F. Rahman, Y. Mitani, M. Watanabe, Robust virtual inertia control of an islanded microgrid considering high penetration of renewable energy, IEEE Access 6 (2018) 625–636, http://dx.doi.org/10.1109/ACCESS.2017.2773486.

[7] S. Oh, S. Chae, J. Neely, J. Baek, M. Cook, Efficient model predictive control strategies for resource management in an islanded microgrid, Energies 10 (2017) 1008, http://dx.doi.org/10.3390/en10071008.

[8] Z. Rostami, S.N. Ravadanegh, N.T. Kalantari, J.M. Guerrero, J.C. Vasquez, Dynamic modeling of multiple microgrid clusters using regional demand response programs, Energies 13 (16) (2020) http://dx.doi.org/10.3390/en13164050.

[9] K. Sabah, H. Nguyen, T. Mahmoud, S. Jayasinghe, J. Guerrero, Optimal sizing of battery energy storage systems for dynamic frequency control in an islanded microgrid: A case study of Flinders Island, Australia, Energy (2020) 117059, http://dx.doi.org/10.1016/j.energy.2020.117059.

[10] Y. Zhang, N. Gatsis, G.B. Giannakis, Robust energy management for microgrids with high-penetration renewables, IEEE Trans. Sustain. Energy 4 (4) (2013) 944–953.

[11] P. Fortenbacher, J.L. Mathieu, G. Andersson, Modeling and optimal operation of distributed battery storage in low voltage grids, IEEE Trans. Power Syst. 32 (6) (2017) 4340–4350, http://dx.doi.org/10.1109/TPWRS.2017.2682339, arXiv:1603.06468.

[12] T. Dragičević, H. Pandžić, D. Škrlec, I. Kuzle, J.M. Guerrero, D.S. Kirschen, Capacity optimization of renewable energy sources and battery storage in an autonomous telecommunication facility, IEEE Trans. Sustain. Energy 5 (4) (2014) 1367–1378, http://dx.doi.org/10.1109/TSTE.2014.2316480.

[13] R. Machlev, N. Zargari, N.R. Chowdhury, J. Belikov, Y. Levron, A review of optimal control methods for energy storage systems - energy trading, energy balancing and electric vehicles, J. Energy Storage 32 (2020) 101787, http://dx.doi.org/10.1016/j.est.2020.101787.

[14] H. Bevrani, Robust Power System Frequency Control, in: Power Electronics and Power Systems, Springer International Publishing, Cham, 2014, http://dx.doi.org/10.1007/978-3-319-07278-4.

[15] H. Bevrani, B. Francois, T. Ise, Microgrid Dynamics and Control, John Wiley & Sons, Inc., Hoboken, NJ, USA, 2017, http://dx.doi.org/10.1002/9781119263739.

[16] L. Meegahapola, Characterisation of gas turbine dynamics during frequency excursions in power networks, IET Gener. Transm. Distrib. 8 (10) (2014) 1733–1743, http://dx.doi.org/10.1049/iet-gtd.2013.0824, _eprint: https://onlinelibrary.wiley.com/doi/pdf/10.1049/iet-gtd.2013.0824.

[17] K. Gubba Ravikumar, B. Bosley, T. Clark, J. Garcia, Generation control system: Using isochronous load-sharing principles with gas and steam turbine generators, IEEE Ind. Appl. Mag. 25 (2) (2019) 36–44, http://dx.doi.org/10.1109/MIAS.2018.2875127, Conference Name: IEEE Industry Applications Magazine.

[18] Z. Rostami, S.N. Ravadanegh, N.T. Kalantari, J.M. Guerrero, J.C. Vasquez, Dynamic modeling of multiple microgrid clusters using regional demand response programs, Energies 13 (16) (2020) 4050, http://dx.doi.org/10.3390/en13164050, Number: 16 Publisher: Multidisciplinary Digital Publishing Institute.

[19] P.C. Sahu, S. Mishra, R.C. Prusty, S. Panda, Improved-salp swarm optimized type-II fuzzy controller in load frequency control of multi area islanded AC microgrid, Sustain. Energy Grids Netw. 16 (2018) 380–392, http://dx.doi.org/10.1016/j.segan.2018.10.003.

[20] V.P. Singh, S.R. Mohanty, N. Kishor, P.K. Ray, Robust H-infinity load frequency control in hybrid distributed generation system, Int. J. Electr. Power Energy Syst. 46 (2013) 294–305, http://dx.doi.org/10.1016/j.ijepes.2012.10.015.

[21] H. Bevrani, M.R. Feizi, S. Ataee, Robust frequency control in an islanded microgrid: H_∞ and μ -synthesis approaches, IEEE Trans. Smart Grid 7 (2) (2016) 706–717, http://dx.doi.org/10.1109/TSG.2015.2446984, Conference Name: IEEE Transactions on Smart Grid.

[22] T. Kerdphol, F.S. Rahman, Y. Mitani, M. Watanabe, S.K. Küfeoğlu, Robust virtual inertia control of an islanded microgrid considering high penetration of renewable energy, IEEE Access 6 (2018) 625–636, http://dx.doi.org/10.1109/ACCESS.2017.2773486, Conference Name: IEEE Access.

[23] A.M. Ersdal, L. Imsland, K. Uhlen, Model predictive load-frequency control, IEEE Trans. Power Syst. 31 (1) (2016) 777–785, http://dx.doi.org/10.1109/TPWRS.2015.2412614, Conference Name: IEEE Transactions on Power Systems.

[24] T. Yang, Y. Zhang, Z. Wang, H. Pen, Secondary frequency stochastic optimal control in independent microgrids with virtual synchronous generator-controlled energy storage systems, Energies 11 (9) (2018) 2388, http://dx.doi.org/10.3390/en11092388.

[25] M.-R. Chen, G.-Q. Zeng, Y.-X. Dai, K.-D. Lu, D.-Q. Bi, Fractional-order model predictive frequency control of an islanded microgrid, Energies 12 (1) (2018) 84, http://dx.doi.org/10.3390/en12010084.

[26] S. Jain, Y.V. Hote, Design of fractional PID for Load frequency control via Internal model control and Big bang Big crunch optimization, IFAC-PapersOnLine 51 (4) (2018) 610–615, http://dx.doi.org/10.1016/j.ifacol.2018.06.163.

[27] J. Singh, K. Chattterjee, C. Vishwakarma, Two degree of freedom internal model control-PID design for LFC of power systems via logarithmic approximations, ISA Trans. 72 (2018) 185–196, http://dx.doi.org/10.1016/j.isatra.2017.12.002.

[28] P. Patrinos, S. Trimboli, A. Bemporad, Stochastic MPC for real-time market-based optimal power dispatch, in: 2011 50th IEEE Conference on Decision and Control and European Control Conference, IEEE, 2011, pp. 7111–7116.

[29] E. González Querubín, J. Sanchis, S. Garcia-Nieto Rodriguez, J. Salcedo, A comparative study of stochastic model predictive controllers, Electronics 9 (2020) 2078, http://dx.doi.org/10.3390/electronics9122078.

[30] S. Di Cairano, D. Bernardini, A. Bemporad, I.V. Kolmanovsky, Stochastic MPC with learning for driver-predictive vehicle control and its application to HEV energy management, IEEE Trans. Control Syst. Technol. 22 (3) (2014) 1018–1031.

[31] H. Bevrani, M.R. Feizi, S. Ataee, Robust frequency control in an islanded microgrid: H_∞ and μ -synthesis approaches, IEEE Trans. Smart Grid 7 (2) (2016) 706–717, http://dx.doi.org/10.1109/TSG.2015.2446984.

[32] Kundur, [Prabha Kundur] Power System Stability and Control.Pdf.

[33] C. Gavriluta, S. Spataru, I. Mosincat, C. Citro, I. Candela, P. Rodriguez, Complete methodology on generating realistic wind speed profiles based on measurements, REPQJ (2012) 1757–1762, http://dx.doi.org/10.24084/repqj10.828.

[34] International Standard IEC 61400-1, Tech. Rep.

[35] J.F. Manwell, J.G. McGowan, Lead acid battery storage model for hybrid energy systems, Sol. Energy 50 (5) (1993) 399–405.

[36] P. Fortenbacher, J.L. Mathieu, G. Andersson, Modeling, identification, and optimal control of batteries for power system applications, in: 2014 Power Systems Computation Conference, 2014, pp. 1–7, http://dx.doi.org/10.1109/PSCC.2014.7038360.

[37] P. Fortenbacher, J.L. Mathieu, G. Andersson, Modeling and optimal operation of distributed battery storage in low voltage grids, IEEE Trans. Power Syst. 32 (6) (2017) 4340–4350, http://dx.doi.org/10.1109/TPWRS.2017.2682339.

[38] W. Tan, Unified tuning of PID load frequency controller for power systems via IMC, IEEE Trans. Power Syst. 25 (1) (2010) 341–350, http://dx.doi.org/10.1109/TPWRS.2009.2036463.

[39] Y. Shi, B. Xu, Y. Tan, B. Zhang, A convex cycle-based degradation model for battery energy storage planning and operation, 2017.

[40] G. Calafiore, M. Campi, Robust convex programs: randomized solutions and applications in control, in: 42nd IEEE International Conference on Decision and Control (IEEE Cat. No.03CH37475), vol. 3, 2003, pp. 2423–2428 Vol.3, http://dx.doi.org/10.1109/CDC.2003.1272983.

[41] M.C. Campi, S. Garatti, M. Prandini, Scenario optimization for MPC, in: S.V. Raković, W.S. Levine (Eds.), Handbook of Model Predictive Control, in: Control Engineering, Springer International Publishing, Cham, 2019, pp. 445–463, http://dx.doi.org/10.1007/978-3-319-77489-3_19.

[42] A. Shapiro, D. Dentcheva, A. Ruszczyński, Lectures on Stochastic Programming: Modeling and Theory, Society for Industrial and Applied Mathematics, 2009, http://dx.doi.org/10.1137/1.9780898718751.

[43] M.C. Campi, S. Garatti, M. Prandini, The scenario approach for systems and control design, Annu. Rev. Control 33 (2) (2009) 149–157, http://dx.doi.org/10.1016/j.arcontrol.2009.07.001.

[44] E.F. Camacho, C. Bordons, in: M.J. Grimble, M.A. Johnson (Eds.), Model Predictive Control, in: Advanced Textbooks in Control and Signal Processing, Springer London, London, 2007, http://dx.doi.org/10.1007/978-0-85729-398-5.

[45] Model predictive control system design and implementation using MATLAB®, Advances in Industrial Control, Springer London, London, 2009, http://dx.doi.org/10.1007/978-1-84882-331-0, ISSN:1430-9491.

[46] S. Skogestad, Multivariable Feedback Control : Analysis and Design, second ed., Wiley, Chichester, 2005.

[47] A.M. Ersdal, L. Imsland, K. Uhlen, D. Fabozzi, N.F. Thornhill, Model predictive load–frequency control taking into account imbalance uncertainty, Control Eng. Pract. 53 (2016) 139–150, http://dx.doi.org/10.1016/j.conengprac.2015.12.001.

[48] S. Garatti, M.C. Campi, Modulating robustness in control design: Principles and algorithms, IEEE Control Syst. Mag. 33 (2) (2013) 36–51, http://dx.doi.org/10.1109/MCS.2012.2234964, Conference Name: IEEE Control Systems Magazine.